Available online at www.sciencedirect.com

SciVerse ScienceDirect

Ceramics International 39 (2013) 4191–4204

CERAMICS INTERNATIONAL

www.elsevier.com/locate/ceramint

On the enhancement of the spark-plasma sintering kinetics of ZrB_2–SiC powder mixtures subjected to high-energy co-ball-milling

Victor Zamora[a], Angel L. Ortiz[a,*], Fernando Guiberteau[a], Mats Nygren[b]

[a]Departamento de Ingeniería Mecánica, Energética y de los Materiales, Universidad de Extremadura, 06006 Badajoz, Spain
[b]Department of Materials and Environmental Chemistry, University of Stockholm, 10691 Stockholm, Sweden

Received 15 October 2012; received in revised form 31 October 2012; accepted 1 November 2012
Available online 7 November 2012

Abstract

The spark-plasma sintering (SPS) kinetics of ZrB_2–SiC powder mixtures was investigated as a function of the degree of high-energy co-ball-milling and of the SiC content (5, 17.5, or 30 vol%). As in ZrB_2 without SiC, it was found that the crystal size refinement induced by the continued milling progressively enhances the SPS kinetics of ZrB_2–SiC, again only moderately if the refinement is to the ultra-fine range, but very marked if the refinement is to the nanoscale. It was also found that the SiC addition further enhances the SPS kinetics of ZrB_2, although the improvement did not scale directly with the SiC content, and became less relevant with the refinement of the ZrB_2 crystal sizes to the nanoscale. The improved kinetics induced by the SiC addition was identified as being due to the formation of amorphous borosilicate from the oxide passivating layers on the ZrB_2 and SiC particles. This not only speeds up the interparticle diffusion, but also it is segregated under the application of pressure into the multi-grain joints, filling pores. The enhanced kinetics induced by the progressive milling is due to the continuous reduction of the diffusion distances and to the development of a greater density of grain boundaries available as faster diffusion paths, together with the greater formation of amorphous borosilicate. Implications of interest for the ultra-high-temperature ceramics community are discussed.

Keywords: ZrB_2; Ultra-high-temperature ceramics; Spark-plasma sintering; High-energy ball-milling

1. Introduction

ZrB_2 with SiC additions is one of the few materials to have captured the attention of the ultra-high-temperature ceramic (UHTC) community. This is because these composites combine efficiently the attractive ultra-refractory properties and relatively low density of the ZrB_2 matrices with the beneficial role of the SiC improving the oxidation resistance and the mechanical properties [1,2]. Not surprisingly, the last few years have seen a flurry of research activity aimed at studying the ZrB_2–SiC composites in detail [1–36], much of which has centred on their conventional pressureless sintering and hot-pressing at lower temperatures. More recently, the development of spark-plasma sintering (SPS) has also motivated a growing interest in their rapid lower-temperature densification with finer microstructures [2,37–47], with the anticipation of further improvement of the mechanical properties. Note that this rapid densification is beyond the possibilities of both conventional pressureless sintering and hot-pressing, since they are based on the use of radiant heating elements; furthermore, microwave sintering has fundamental problems in the case of ZrB_2—a very good conductor that does not readily couple with microwaves—and the viability of flash sintering ZrB_2 has yet to be demonstrated.

Another field of particular current attention within the UHTC community is the study of the dependence of the sinterability of these materials on the processing method used for the starting powders, because it is now known that the features of the starting powders strongly condition the driving force for their densification [1,2,17,45,48,49]. The ZrB_2–SiC powder mixtures for SPS are no exception to this general rule, as has been demonstrated recently in two comparative densification studies, one performed on

*Corresponding author: Tel.: +34 924289600x86726; fax: +34 924289601.
E-mail addresses: alortiz@unex.es, alortiz@materiales.unex.es (A.L. Ortiz).

0272-8842/$ - see front matter © 2012 Elsevier Ltd and Techna Group S.r.l. All rights reserved.
http://dx.doi.org/10.1016/j.ceramint.2012.11.001

powders in the as-received condition and after attrition milling (these latter with and without intentional oxidation and carbon addition [45]), and the other on powders subjected to conventional ball-milling or attrition milling, with and without subsequent heat-treatment for oxide elimination [47]. Clearly, more fundamental studies of this kind are required to extend our knowledge of the effects of the powder processing methods on the densification by SPS of the ZrB_2–SiC composites.

A recent advance in the powder processing area of UHTCs is high-energy ball-milling under dry conditions, which is able to refine ZrB_2 powders and ZrB_2–SiC powder mixtures to the nanoscale [50–52]; note that this is something that cannot be done by conventional ball-milling or wet attrition milling because neither of them generate the high compressive stresses required to fracture ultra-fine particles [53,54]. However, systematic investigation of the effects of high-energy ball-milling on the sinterability of ZrB_2-based powders is very limited, the exception being two studies devoted to investigating the SPS kinetics [55] and densification [56] of ZrB_2 powders as a function of milling time. Consequently, as a continuation to these previous studies, the present work was undertaken to investigate for the first time the improvement of the SPS kinetics of the typical ZrB_2–SiC powder mixtures (i.e., 5–30 vol% of SiC) induced by high-energy co-ball milling. The study is therefore focused exclusively on processing aspects, with the detailed investigation of materials properties deferred to later reports.

2. Experimental procedure

The preparation protocol of the three sets of ZrB_2–SiC powder mixtures with eight different degrees of high-energy co-ball milling[1] each which were used in the present study has been described in detail elsewhere [52]. Consequently, we shall describe here only the key steps. Briefly, commercially-available ZrB_2 (Grade B, H.C. Starck, Germany; ~2–3 μm) and SiC (UF-15, H.C. Starck, Germany; ~0.55 μm) powders combined in relative concentrations of 95–5, 82.5–17.5, and 70–30 vol%, respectively, were co-milled in air for different times (i.e., 1, 3, 5, 10, 30, 60, and 180 min) in a shaker mill (Spex D8000, Spex CertiPrep, USA) operated at 1060 back-and-forth cycles per minute. The milling was carried out in a cylindrical hardened-steel container with WC balls (6.7 mm in diameter; Union Process Inc., USA) under a ball-to-powder weight ratio of 4, using the procedure described elsewhere to minimize the contamination from the milling media and container [56]. ZrB_2–SiC powder mixtures without co-milling were also prepared following the conventional method of wet homogenization plus drying of the slurries under stirring. The microstructural features of all these ZrB_2–SiC powder mixtures have been investigated in detail by X-ray diffractometry (XRD), scanning electron microscopy (SEM), and laser scattering (LS) in an earlier publication [52], where the evolution of the ZrB_2 crystal sizes and of the particle sizes with the milling time as a function of the SiC content was also discussed comprehensively. Consequently, these crystal and particle size data will be used here directly without repeating their presentation or discussion. Nevertheless, the earlier microstructural characterization study has been completed with the analysis of selected ZrB_2–SiC powder mixtures by X-ray photoemission spectroscopy (XPS) for the determination of the bonding status. The XPS spectra were recorded under ultra-high vacuum (10^{-6} Pa) using a high-resolution spectrometer (K-Alpha, Thermo Scientific, UK) equipped with a monochromatic Al-Kα X-ray source (1486.6 eV), and making two types of measurement: (1) survey scans in the 0–1350 eV range at 1 eV resolution, and (2) detailed scans in the 96–110 and 177–195 eV ranges at 0.1 eV energy resolution, which cover the Si 2p, and the Zr 3d and B 1s core lines, respectively.

All ZrB_2–SiC powder mixtures were individually loaded into 12-mm diameter graphite dies lined with graphite foil and surrounded by a 1-cm thick graphite blanket to minimize the heat loss, and were then spark-plasma sintered (Dr. Sinter SPS-2050, Sumitomo Coal Mining Co., Japan) in dynamic vacuum up to 1750 °C. The graphite die has a wall thickness of 9 mm, and has a hole machined in its central region of 2.5 mm depth. The temperature was first raised manually to 600 °C in 3 min, and thence onwards was measured by an optical pyrometer focused on the interior of hole of the graphite die. The heating ramp was set at 200 °C min^{-1} up to 1200 °C, and thence onwards at only 100 °C min^{-1} to capture more accurately the characteristic points of the SPS curves. The uniaxial pressure was 50 MPa up to 1200 °C, and 75 MPa thenceforth. The soaking at 1750 °C was interrupted when the punches ceased travelling, at which moment the load was released and the electrical power was shut off.

The shrinkage curves measured experimentally with the dilatometer of the SPS furnace were then corrected for the expansion of the graphite parts to obtain the real shrinkage curve of the powders themselves, and next converted to densification curves using the relative densities of the sintered materials. Selected UHTCs resulting from these SPS cycles were characterized using SEM, X-ray energy dispersive spectrometry (XEDS), and XRD. The SEM observations were mostly made on fracture surfaces, and sporadically on polished surfaces, without additional preparation, using either a conventional microscope (S-3600N, Hitachi, Japan) or a field-emission (FE) microscope (S-4800II, Hitachi, Japan). The XEDS analyses were carried out under the FE-SEM, essentially to map the distribution of elemental Zr (line $L\alpha_1$ at 2.040 keV), Si (line $K\alpha_1$ at 1.739 keV), C (line $K\alpha_1$ at 0.266 keV), and O (line $K\alpha_1$ at 0.517 keV), although spectra in spot mode were also collected occasionally. B was not mapped because this light element is at the detection limit of the spectrometer,

[1] Hereafter, the term high-energy (co-)ball-milling will be abbreviated simply as (co-)milling for the sake of readability.

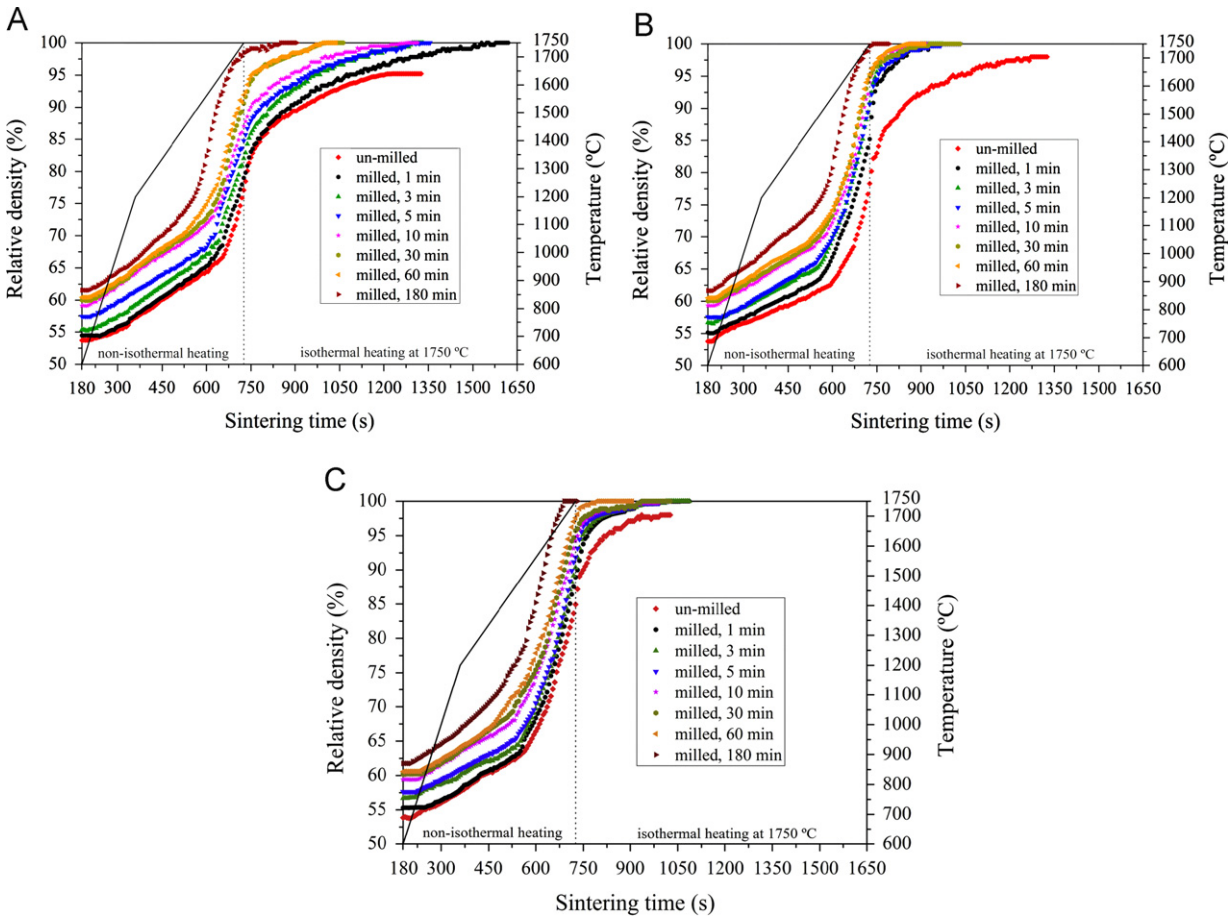

Fig. 1. SPS-densification curves as a function of time for the ZrB_2–SiC powder mixtures with different degrees of high-energy co-ball-milling and SiC additions of: (A) 5 vol%, (B) 17.5 vol%, and (C) 30 vol%. The points are the experimental data. The solid line indicates the temperature profile used. The dashed line separates the regimes of non-isothermal and isothermal heating during the SPS cycle.

and in addition its $K\alpha_1$ line (at 0.172 keV) severely overlaps with the $M\alpha_1$ line of Zr (at 0.152 keV), thus introducing an unnecessary uncertainty into the measurements. W was not mapped either, because the WC contamination introduced during milling is very low (i.e., less than 0.5 vol%) [56]. Finally, the XRD patterns were acquired in step-scanning mode (measurement range 22–62° 2θ, step width 0.028° 2θ, and count time 3 s/step) using a high-resolution laboratory diffractometer (D8 Advance, Bruker AXS, Germany) equipped with a primary monochromator that provides pure $CuK\alpha_1$ radiation ($\lambda = 1.5406$ Å) and a linear ultra-fast detector. The phases present were identified with the aid of the PDF2 database.

3. Results

3.1. Kinetics of SPS

Fig. 1 shows the SPS densification curves as functions of time for the three sets of ZrB_2–SiC powder mixtures. It can be seen that they all have the same general shape regardless of the milling time and SiC content. Specifically, first the powder always compacts linearly, then at a certain sintering time rapidly consolidates while the furnace continues heating up to 1750 °C, and lastly the compaction slows down to eventually reach the ultimate degree of densification. Nevertheless, the mere comparison of the curves in Fig. 1 indicates clearly that SPS kinetics benefits from the increase in SiC content and milling time. To illustrate this kinetics enhancement more rigorously, we compared various characteristic points of these densification curves with each other and, when possible, also with those determined before for the ZrB_2 without SiC [55]. These are:[2] (i) the degree of densification at the beginning of the SPS cycle (ρ_0); (ii) the onset temperature of sintering (T_{OS}), which is the temperature at which the densification curve first deviates from the linear compaction stretch due to the activation of diffusion; (iii) the onset temperature of the intermediate stage of sintering (T_{OIS}), which is the sintering regime in which the pore distribution transforms from open porosity to closed porosity and is typically taken to begin at ~70% relative density [57]; (iv) the peak

[2]Temperatures will be given if the characteristic point of the densification curve falls within the regime of non-isothermal heating for the three ZrB_2–SiC powder mixtures and milling time including the un-milled case. Otherwise, sintering times will be reported.

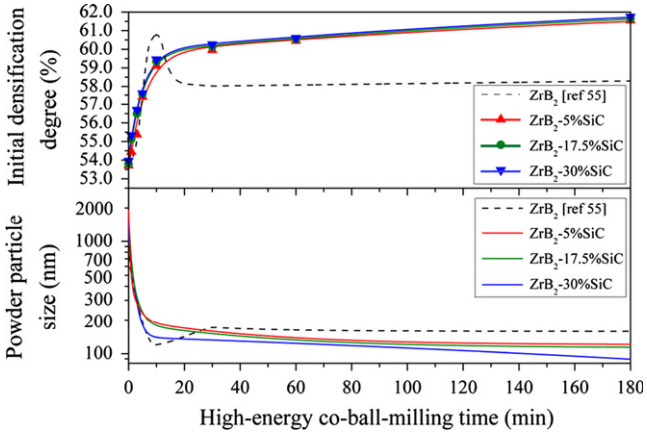

Fig. 2. Degrees of densification at the beginning of the SPS cycle for the ZrB_2–SiC powder mixtures (5, 17.5, or 30 vol% SiC) as a function of the high-energy co-ball-milling time. The points are the experimental data, and the solid lines are merely to guide the eye. The dashed line is for ZrB_2 without SiC addition (taken from Ref. [55]). Also included is the average particle size in the different ZrB_2–SiC powder mixtures and in the ZrB_2 powder as determined by laser scattering (taken from Ref. [55]).

temperature in the shrinkage-rate curves (T_{MSC}), which is the temperature at which the best combination of active densification mechanisms occurs; (v) the onset time of the final stage of sintering (t_{OFS}), which is the sintering regime in which the closed porosity is eliminated, and is normally taken to commence at ~90% relative density [57]; and finally (vi) the sintering time required to reach complete or near-complete densification (t_{FD}).

Fig. 2 compares the evolution of ρ_0 with the milling time for the three ZrB_2–SiC powder mixtures and for the ZrB_2 powder [55]. There are various interesting features in this figure. Firstly, ρ_0 increases continuously although very little (i.e., less than 1.33%) with increasing SiC content in the ZrB_2–SiC powder mixtures from 5 to 30 vol%. Secondly, except for the intermediate milling times (i.e., 7 to 20 min), the ZrB_2–SiC powder mixtures compacted better than the ZrB_2 powder, a phenomenon that was more pronounced for long milling times (i.e., ~3.5% at 180 min of milling). And thirdly, the three ZrB_2–SiC powder mixtures exhibit a simple trend, with ρ_0 increasing continuously as the milling time increases, which is substantially different from the ZrB_2 powder that first displays an increase and then a decrease. As also shown in Fig. 2, all these trends are determined by the particle sizes in these powders because in powder compacts particle size and pore size scale together at the beginning of the sintering process [58]. Note that the evolution of the particle sizes differs because SiC alters the rates of fracture and of cold-welding of ZrB_2 during the milling, as is explained in more detail in an earlier publication [52].

Fig. 3 compares the evolution of T_{OS}, T_{OIS}, T_{MSC}, t_{OFS}, and t_{FD} with the ZrB_2 crystal size achieved during the milling for the three ZrB_2–SiC powder mixtures and, when possible, also for the ZrB_2 powder [55]. It can be seen that these magnitudes all decrease progressively with decreasing ZrB_2 crystal size and also with increasing SiC content, thus confirming the deductions made from the mere observation of the densification curves in Fig. 1. Also very interesting is that these five plots show that, for a given SiC content, the enhancement of the SPS kinetics is always only moderate with the refinement of the ZrB_2 crystal size to the ultra-fine range, but very marked with the refinement to the nanometre range. The dependence on the SiC content is more complex. Firstly, just 5 vol% SiC is sufficient to appreciably speed up the ZrB_2 densification, even in the un-milled condition. Secondly, the kinetics enhancement does not scale directly with the SiC content, but tends to saturate as this increases; for example, consider that the reductions in T_{OS}, T_{OIS}, T_{MSC}, t_{OFS}, and t_{FD} achieved with the addition of 5 and 30 vol% SiC do not reflect any 6-fold difference between the values, and, in addition, there is greater kinetics enhancement when the SiC content was increased from 5 to 17.5 vol% than from 17.5 to 30 vol% despite the SiC content increasing by 12.5 vol% in both cases. And thirdly, the beneficial role of the SiC addition decreases in relevance with the progressive refinement of the ZrB_2 crystal size, especially at the nanoscale. Taken together, these observations suggest a change in the densification mechanism of the ZrB_2–SiC powder mixtures in relation to the ZrB_2 powder.

3.2. Microstructure after SPS

Fig. 4 shows representative FE-SEM micrographs of the UHTC resulting from the ZrB_2–30%SiC powder mixture milled for 180 min, which has the best SPS kinetics of all those investigated here. It can be observed in Fig. 4A that this material is completely dense, as there is no evidence of residual porosity. At this temperature, ZrB_2 without SiC but with the same milling time has reached only ~90% relative density [55]. It can also be seen in Fig. 4A that the microstructure consists of a mixture of various types of grains. Specifically, there are micrometre grains with equiaxed shape, which form the primary matrix. There are also submicrometre grains distributed uniformly in the matrix. And lastly, there are rounded grains with much smoother surfaces and ultra-fine size which are segregated between the micrometre and submicrometre grains and whose morphology suggests that they originated from the solidification of a viscous phase. As can be seen in the FE-SEM micrograph of Fig. 4B, the observation of the polished surface corroborates the microstructural information deduced from the fracture surface. In the backscattered-electron FE-SEM micrograph of Fig. 4C the micrometre grains and a few of the ultra-fine ones display a marked compositional contrast, indicating that they contain heavier chemical elements than the rest of the grains; the submicrometre grains and the vast majority of the ultra-fine ones exhibit a similar compositional contrast, suggestive of certain similarity between them. Furthermore,

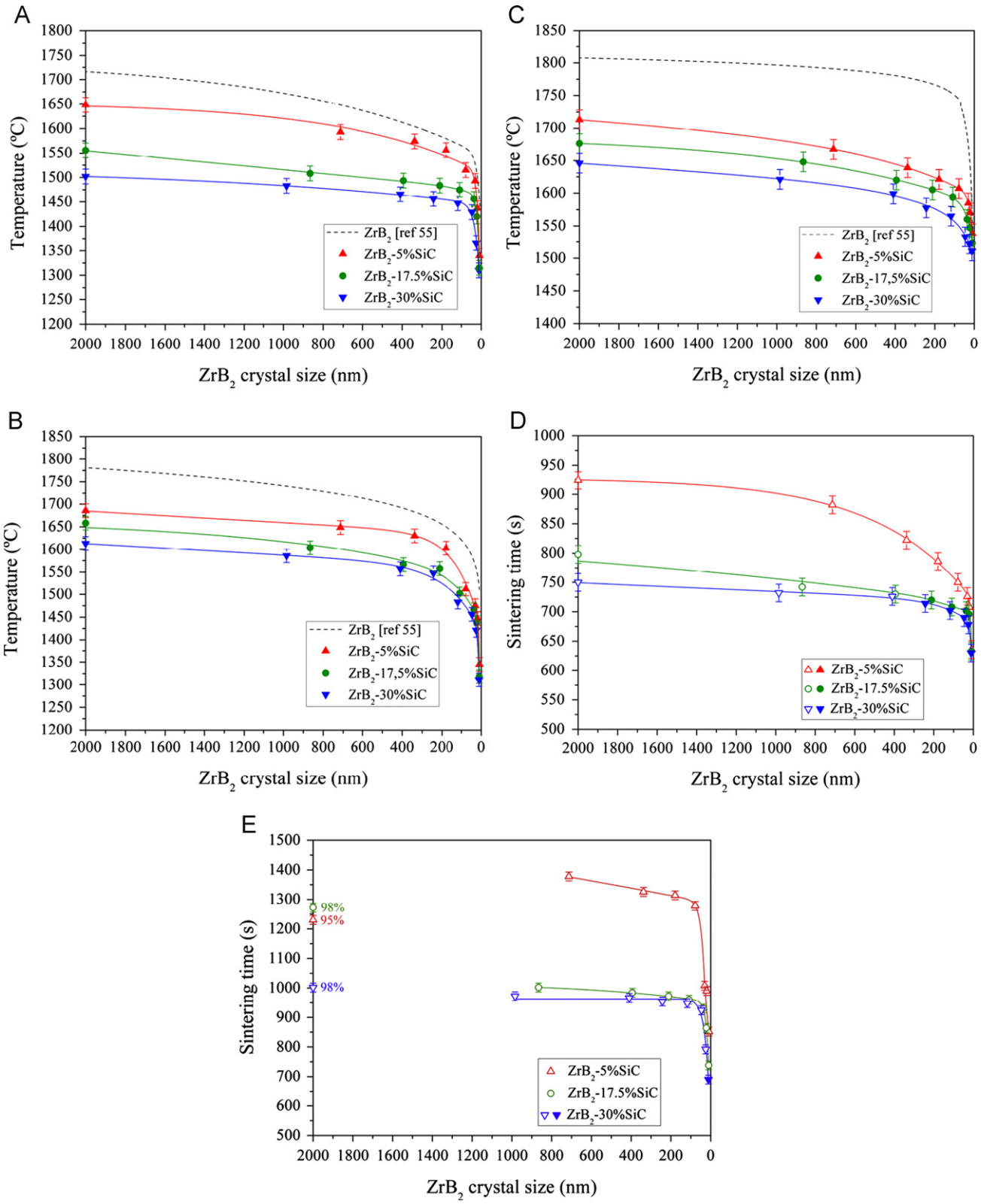

Fig. 3. Evolution of (A) T_{OS}, (B) T_{OIS}, (C) T_{MSC}, (D) t_{OFS}, and (E) t_{FD} with the ZrB_2 crystal size achieved during the milling for the ZrB_2–SiC powder mixtures (5, 17.5, or 30 vol% SiC). The points are the experimental data, and the lines are merely to guide the eye. The open symbols are values of t_{OFS} and t_{FD} determined under isothermal heating at 1750 °C, and not under non-isothermal heating as in the rest of the cases. Temperature data for the ZrB_2 powders without SiC have also been included as dashed lines (taken from Ref. [55]) because the heating ramp was the same as used here; the sintering time data have not been compared with those of ZrB_2 powders because they are affected by the isothermal soakings at different temperatures (i.e., 1750 and 1900 °C with and without SiC addition, respectively).

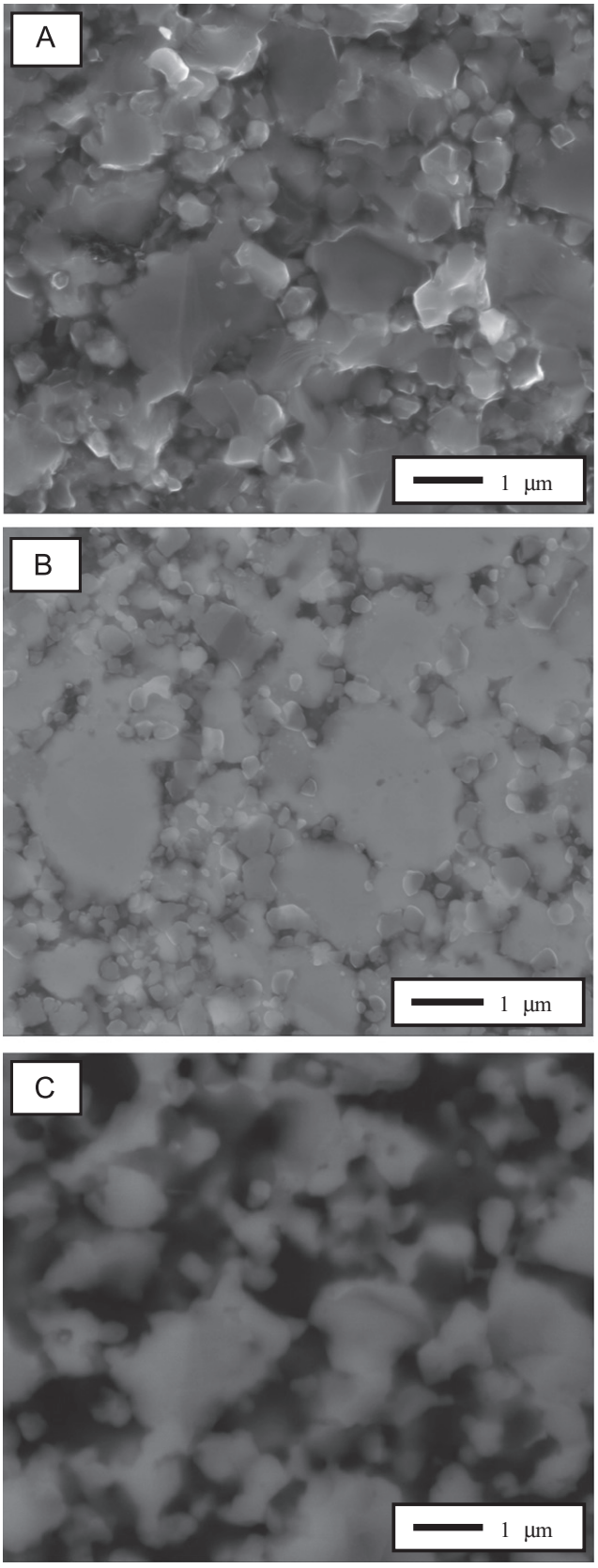

Fig. 4. FE-SEM micrographs of the UHTC resulting from the SPS at 1750 °C for 0 min of the ZrB_2–30%SiC powder mixture subjected to 180 min of high-energy co-ball-milling. (A) Secondary-electron image of the fracture surface, (B) secondary-electron image of the polished surface, and (C) backscattered-electron image of the fracture surface.

the size of the grains in Fig. 4A–C reveals the occurrence of marked coarsening induced by diffusion because this powder mixture consisted of ultrafine agglomerates (i.e., ~100 nm) of nano-particles (i.e., ~10 nm) [52].

Fig. 5 shows the compositional maps of elemental Zr, Si, C, and O obtained by XEDS under the FE-SEM to identify the chemical nature of the different types of grains observed in Fig. 4A. It can be concluded from the Zr distribution that the micrometre grains that form the matrix are ZrB_2. The submicrometre grains are SiC, as proved by the overlap of the Si and C signals. And lastly, the ultra-fine grains are mostly borosilicate and ZrO_2 at a much smaller proportion. Note that the ambiguity between borosilicate and SiO_2 was broken by XEDS analyses in spot mode (not shown), which revealed a clear deviation from the SiO_2 stoichiometry. Finally, Fig. 6 shows the XRD analysis carried out to determine the crystalline or amorphous nature of the phases deduced from the FE-SEM/XEDS analyses. As can be observed, besides the expected ZrB_2 and SiC (6H, 15R, and 4H polytypes) peaks there only appear peaks from ZrO_2 (monoclinic and tetragonal polymorphs) and WC. Therefore, it can be concluded that ZrB_2, SiC, and ZrO_2 are crystalline, while the borosilicate is glassy, as also might be part of the ZrO_2 formed [59]. It is also worth noting that the ZrB_2 and SiC peaks are not shifted from their reference position, which rules out the formation of solid solutions.

Fig. 7 shows a representative FE-SEM micrograph and the corresponding compositional maps of elemental Zr, Si, C, and O for the UHTC resulting from the un-milled ZrB_2–30%SiC powder mixture, and Fig. 8 shows its XRD pattern. The combination of FE-SEM, XEDS, and XRD analyses indicates that the microstructure is formed by fine grains of crystalline SiC, amorphous ZrO_2, and amorphous borosilicate in a matrix of large grains of crystalline ZrB_2. Again, the grain sizes reveal diffusion-induced coarsening because the starting sizes were ~2 μm for ZrB_2 and ~0.55 μm for SiC. It is also evident that there is vast difference in the microstructural scales (factor of ~2.5) of the UHTCs made from the ZrB_2–30%SiC powder mixture in its as-received condition and with 180 min of milling. Therefore, it can be said that the microstructures in Figs. 4 and 7 are qualitatively similar, of course except for WC because one powder mixture was milled and the other was not. In quantitative terms the clear difference is, however, that without milling there is less formation of oxides (i.e., borosilicate plus ZrO_2), the microstructure is less refined, and there persists some slight residual porosity.

Fig. 9 shows typical SEM micrographs of the UHTCs resulting from the ZrB_2–5%SiC and ZrB_2–17.5%SiC powder mixtures with extreme milling times (i.e., 0 and 180 min). Comparison of these SEM images with each other and with those shown in Figs. 4 and 7 for ZrB_2–30%SiC shows that the increase in milling time and in SiC content promotes densification, oxide formation, and microstructural refinement despite the greater diffusion.

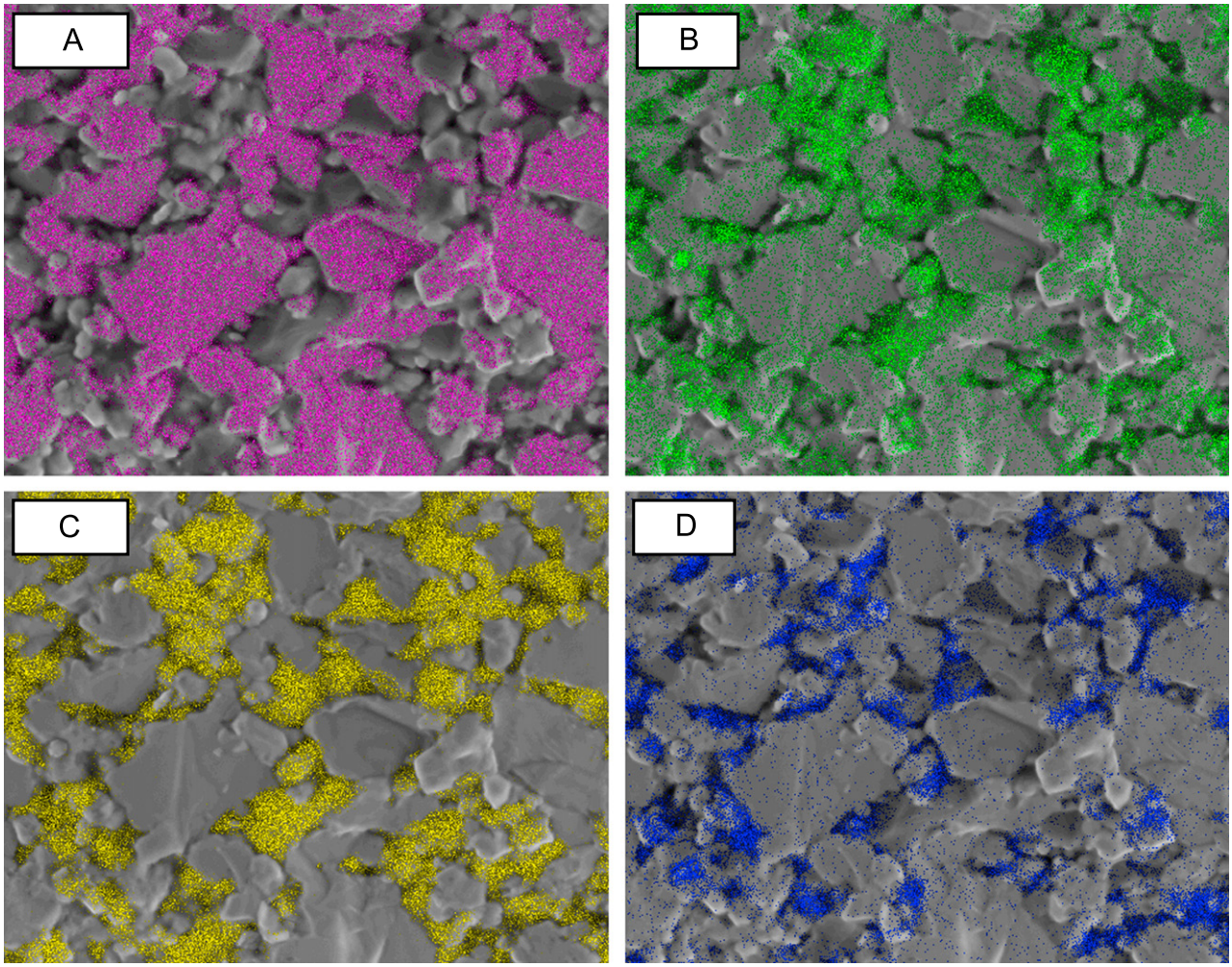

Fig. 5. Compositional mapping of elemental (A) zirconium, (B) carbon, (C) silicon, and (D) oxygen corresponding to the FE-SEM micrograph of Fig. 4A. See Fig. 4A for the bar scale. W was not mapped, but the detection of C-rich particles without overlap with the Si and Zr signals suggests the existence of sparse WC particles.

4. Discussion

The results demonstrate that the SPS kinetics of the ZrB_2–SiC composites is enhanced with increasing SiC content, and also with increasing milling time. This latter is consistent with what has already been observed in ZrB_2, for which enhancement of the SPS kinetics was explained in the framework of solid-state sintering theory [57] (Herring's scaling law [60]), considering that the progressive crystal size refinement to the nanoscale induced by the milling shortens the diffusion distance of the Zr and B species while promoting the formation of a greater density of grain boundaries available as fast diffusion paths. Clearly, all this also occurs in the ZrB_2–SiC powder mixtures, for which the ZrB_2 crystals are also refined progressively with increasing milling time [57]. However, this mechanism alone does not explain the kinetics enhancement observed in ZrB_2–SiC with increasing SiC content, because SiC slowed down the kinetics of ZrB_2 crystal size refinement [57]; this slowing down is due to the early nanocrystallization of SiC that promotes the consumption of collision energy in the form of frictional sliding, thus reducing the effective compressive stresses acting on the ZrB_2 crystals [52]. On the contrary, considering exclusively the criterion of the ZrB_2 crystal size one would indeed expect the worsening of the SPS kinetics with increasing SiC content. Therefore, apart from the ZrB_2 crystal size refinement, there should be other(s) additional mechanism(s) of kinetics enhancement operating in the ZrB_2–SiC powder mixture whose effectiveness increases with increasing SiC content.

In principle, it might be argued that SiC, driven by its lower refractoriness (melting point of 2730 °C for SiC vs 3250 °C for ZrB_2), plays a direct role in the enhancement of the SPS kinetics of ZrB_2 and thus the greater the SiC content in the ZrB_2–SiC powder mixtures the faster the SPS kinetics. However, this explanation is not very plausible because the SiC contents used here were below the percolation threshold for SiC to form by itself a connected phase that really helps in the densification of ZrB_2 (Figs. 5 and 7), and also because a recent SPS study has demonstrated that the SiC nano-powder with 10 nm

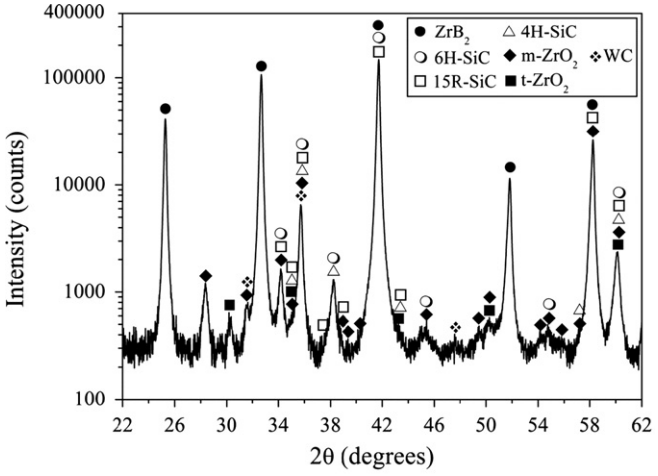

Fig. 6. XRD pattern of the UHTC resulting from the SPS at 1750 °C for 0 min of the ZrB_2–30%SiC powder mixture subjected to 180 min of high-energy co-ball-milling. The phase identification is included (*t* and *m* mean tetragonal and monoclinic, respectively). The logarithmic vertical scale is to facilitate the appreciation of the weak peaks (from 15R-SiC, 4H-SiC, *t*-ZrO_2, *m*-ZrO_2, and WC). The distinction between the SiC polytypes and ZrO_2 polymorphs is simply to carry out a rigorous indexing of the XRD pattern instead of indicating only the compounds present.

crystal size reaches only ~88% relative density at 1800 °C under 100 MPa pressure (which are a temperature and pressure higher than used here) [61].

Another possible mechanism is simply the greater green-body density in the compacts of ZrB_2–SiC with increasing SiC content resulting from the lower agglomerate size [52], which ensures more intimate contact favouring diffusion between powder particles during the first moments of SPS. However, Fig. 2 indicates clearly that this is only a minor effect, and therefore it cannot account for the marked enhancement of the SPS kinetics although it indeed contributes to it.

Nor is interdiffusion between ZrB_2 and SiC the mechanism operating, because the microstructural characterization of the present UHTCs (Figs. 5–8) has ruled out the formation of mixed compounds with Zr and Si, or of solid solutions based on ZrB_2 or SiC.

The WC introduced during milling does not play a role either because the XEDS and XRD analyses ruled out the carbothermal reduction of ZrO_2 by WC; at this regards note that ZrC is one of the reaction products in the carbothermal reduction of ZrO_2 by WC ($ZrO_2+3WC \rightarrow ZrC+3W+2CO(g)$, or $3ZrB_2+6WC+ZrO_2 \rightarrow 4ZrC+6WB+2CO(g)$), and was not observed here. This non-occurrence of carbothermal reduction is reasonable because the WC contamination was less than 0.5 vol%, and is also consistent with other recent SPS studies on ZrB_2 powders [55,56,59] and on ZrB_2–SiC powder mixtures [46] which have not observed carbothermal reduction even for greater WC contamination [46]. Note that, unlike pressureless sintering and hot-pressing, in SPS these reduction reactions are neither kinetically nor thermodynamically favoured, because the reaction times are very limited and the rapid densification of the compacts prevents the CO(g) generated from escaping, thus tipping the reaction in favour of the reactants.

Therefore, the mechanism of kinetics enhancement of ZrB_2 with increasing SiC content has necessarily to be related to the formation of the oxides detected by the SEM and XRD analyses (Figs. 4–9). The presence of oxides in the microstructure of ZrB_2–SiC UHTCs is possible because ZrB_2 and SiC powders passivate spontaneously in contact with air. The surface oxidation of ZrB_2 produces ZrO_2 and B_2O_3, and that of SiC produces SiO_2. To confirm this expectation, selected ZrB_2–SiC powder mixtures were analysed by XPS, which is one of the few techniques capable of detecting thin oxide films on ZrB_2 [62]. Fig. 10 shows the binding energy of the Si 2p, Zr 3d, and B 1s core levels in the ZrB_2–30%SiC powder mixtures with 0, 10, and 180 min of milling. Two sets of Si 2p ($2p_{3/2}$–$2p_{1/2}$ doublet with severe overlapping), Zr 3d ($3d_{5/2}$–$3d_{3/2}$ doublet), and B 1s (singlet) peaks are observed in these XPS spectra, which suggests the existence of two different bonding statuses for the Si, Zr, and B atoms. Both in the un-milled and in the two milled ZrB_2–30%SiC powder mixtures, one set of Si 2p, Zr $3d_{5/2}$, Zr $3d_{3/2}$, and B 1s peaks is located at binding energies of ~100.7, 179.2, 181.5, and 188.2 eV, respectively, values which are due to SiC [63] and ZrB_2 [64]. The other set of peaks appears at higher binding energies of ~103.2, 183.6, 186.0, and 193.2 eV, respectively, which are due to SiO_2 [65], ZrO_2 [64], and B_2O_3 [64]. It can also be seen in Fig. 10 that the SiO_2/SiC, B_2O_3/ZrB_2, and ZrO_2/ZrB_2 peak intensity ratios increase with increasing milling time[3]. Therefore, XPS has unambiguously detected the presence of SiO_2, B_2O_3, and ZrO_2 in the un-milled and milled ZrB_2–30%SiC powder mixtures, and also shows them to be much more abundant as the milling time increases. This trend, which is also valid for the ZrB_2–5%SiC and ZrB_2–17.5%SiC powder mixtures, is due to the increase in specific surface area available for passivation induced by the crystal size refinement. Furthermore, the survey XPS spectra shown in Fig. 11A indicate that the abundance of SiO_2 increases, while those of ZrO_2 and B_2O_3 decrease with increasing SiC content in the ZrB_2 powder;[4] this trend was further confirmed by detailed XPS scans[4], as is shown for convenience in Fig. 11B for SiO_2 because this is the limiting compound for the formation of borosilicate. Note that a recent study with a wide battery of characterization techniques has demonstrated that the ZrO_2 and B_2O_3 are

[3]In particular, using the core levels Si 2p for both SiO_2 and SiC, B 1s for B_2O_3, and Zr $3d_{5/2}$ for both ZrO_2 and ZrB_2, one calculates the SiO_2/SiC, B_2O_3/ZrB_2, and ZrO_2/ZrB_2 peak intensity ratios to be, respectively, 0.16, 0.85, and 2.27 for the un-milled powder, 0.68, 1.11, and 4.46 for the powder milled for 10 min, and 1.41, 1.19, and 9.97 for the powder milled for 180 min.

[4]Note that the intensity of the Si 2p signal in the survey XPS spectra of the powders with 0, 5, 17.5, and 30 vol% SiC is 0, 4000, 11,000, and 22,300 counts, that of the Zr 3d signal is 166,500, 144,500, 109,300, and 105,700 counts, and that of the B 1s signal is 83,800, 78,000, 61,850, and 60,900 counts. Similarly, the intensity of the Si 2p signal from SiO_2 in the detailed XPS spectra is 0, 426, 1250, and 2440 counts.

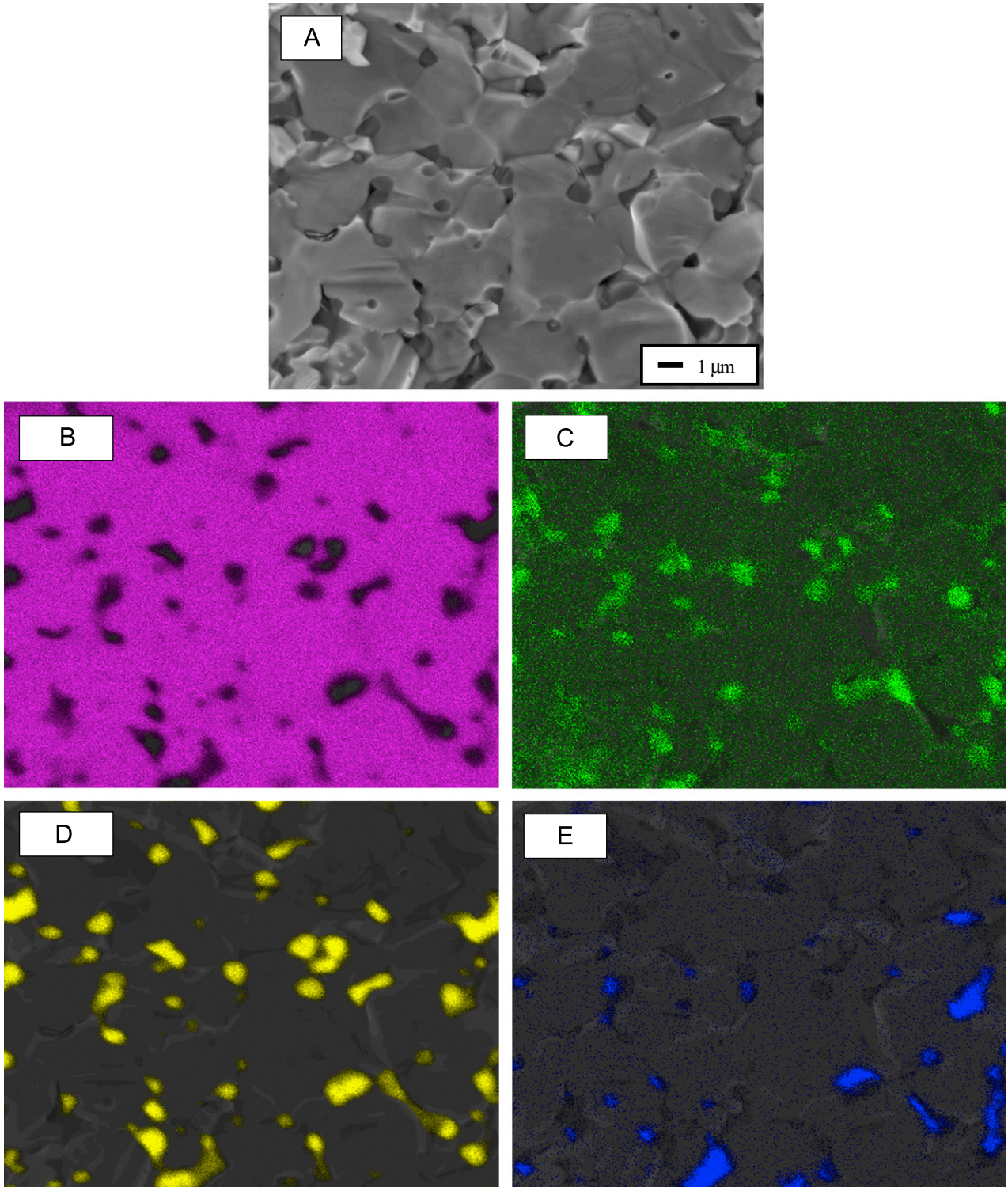

Fig. 7. Microstructure of the UHTC resulting from the SPS at 1750 °C for 5 min of the un-milled ZrB_2–30%SiC powder mixture. (A) FE-SEM micrograph (secondary-electron image of the fracture surface), and the corresponding compositional mapping of elemental (B) zirconium, (C) carbon, (D) silicon, and (E) oxygen.

indeed amorphous [62], which is also the case of SiO_2 because the XRD patterns of the ZrB_2–SiC powder mixtures do not exhibit SiO_2 peaks [52].

Among the two oxides present in the microstructure, ZrO_2 plays at most a very secondary role in the SPS kinetics of the ZrB_2–SiC powder mixtures because it makes two opposite contributions that tend to cancel out. On the one hand, the passivating nano-film of ZrO_2 on the ZrB_2 particles promotes microstructural coarsening, which is detrimental for densification [66,67]. But on the other hand, it also creeps under pressure towards the multi-grain joints, thus filling pores [59], which is beneficial for

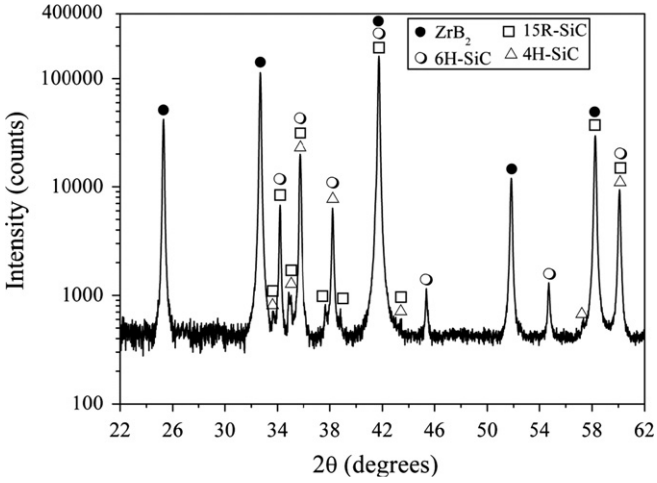

Fig. 8. XRD pattern of the UHTC resulting from the SPS at 1750 °C for 5 min of the un-milled ZrB_2–30%SiC powder mixture. The phase identification is included. The logarithmic vertical scale is to facilitate the appreciation of the weak peaks (from 15R-SiC, and 4H-SiC). The distinction between the SiC polytypes is simply to carry out a rigorous indexing of the XRD pattern instead of indicating only the compounds present.

densification. Thus, the combination of the opposite effects leaves the borosilicate as the primary factor responsible for the enhancement of the SPS kinetics of the ZrB_2 with increasing SiC content.

It is therefore reasonable to think that the underlying mechanism of kinetics enhancement is the following. During the SPS, part of the existing B_2O_3 on the ZrB_2 particles, which normally is highly volatile and escapes from the sample, reacts with the existing SiO_2 on the surface of the neighbouring SiC particles, producing a borosilicate glass that stays in the sample doubly benefiting the SPS kinetics. Firstly, part of the borosilicate forms amorphous nano-films at the interphase grain boundaries, speeding up the interparticle diffusion and therefore enhancing the densification kinetics. Note that the existence of these nano-films has been confirmed elsewhere by high-resolution transmission electron microscopy [16]. And secondly, under the application of high pressures the excess of borosilicate is segregated by viscous flow into the multi-grain joints, thus contributing to the densification by pore filling. This is consistent with independent FE-SEM observations on a ZrB_2–25%SiC UHTCs also fabricated by SPS [47].

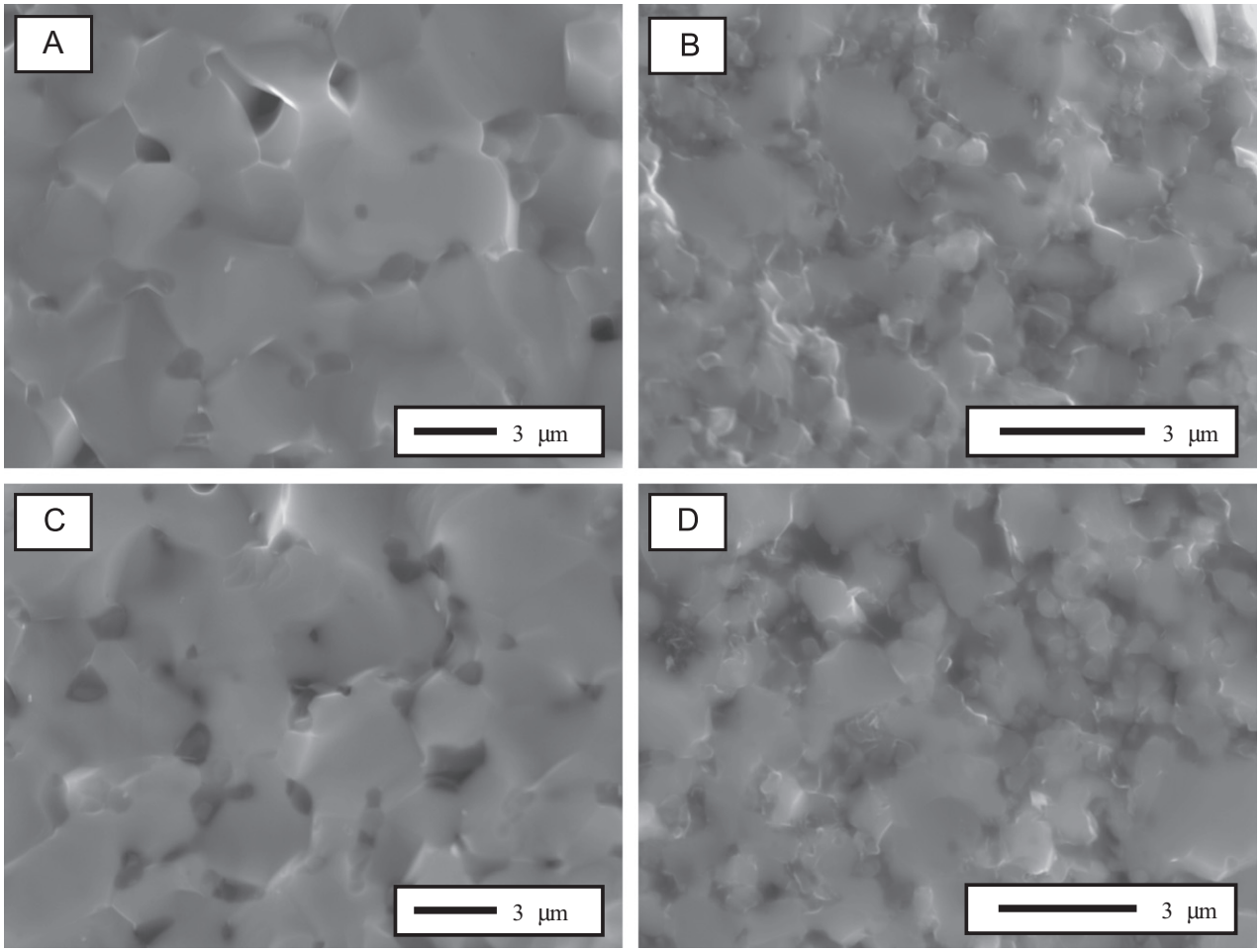

Fig. 9. SEM micrographs (secondary-electron images of the fracture surfaces) of the UHTCs resulting from the SPS at 1750 °C of the ZrB_2–5%SiC powder mixture (A) without and (B) with 180 min of high-energy co-ball-milling, as well as of the ZrB_2–17.5%SiC powder mixture (C) without and (D) with 180 min of high-energy co-ball-milling. The isothermal soakings lasted for 10, 3, 10, and 1 min, respectively.

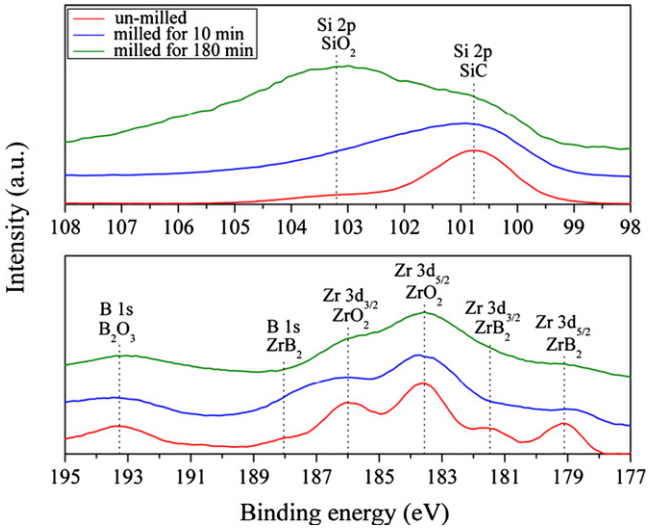

Fig. 10. High-resolution XPS spectra of the Si 2p (doublet Si $2p_{3/2}$–$2p_{1/2}$), Zr 3d (doublet Zr $3d_{5/2}$–$3d_{3/2}$), and B 1s (singlet) core-levels for the ZrB_2–30%SiC powder mixture without and with 10 and 180 min of high-energy co-ball-milling. The peak indexing is included. For the sake of comparison, the XPS spectra have been normalized by imposing the same maximum intensity for the Si 2p peak from SiC, and then shifted along the vertical axis to facilitate their observation. Calculations of peak ratios were made on the original data without shifting.

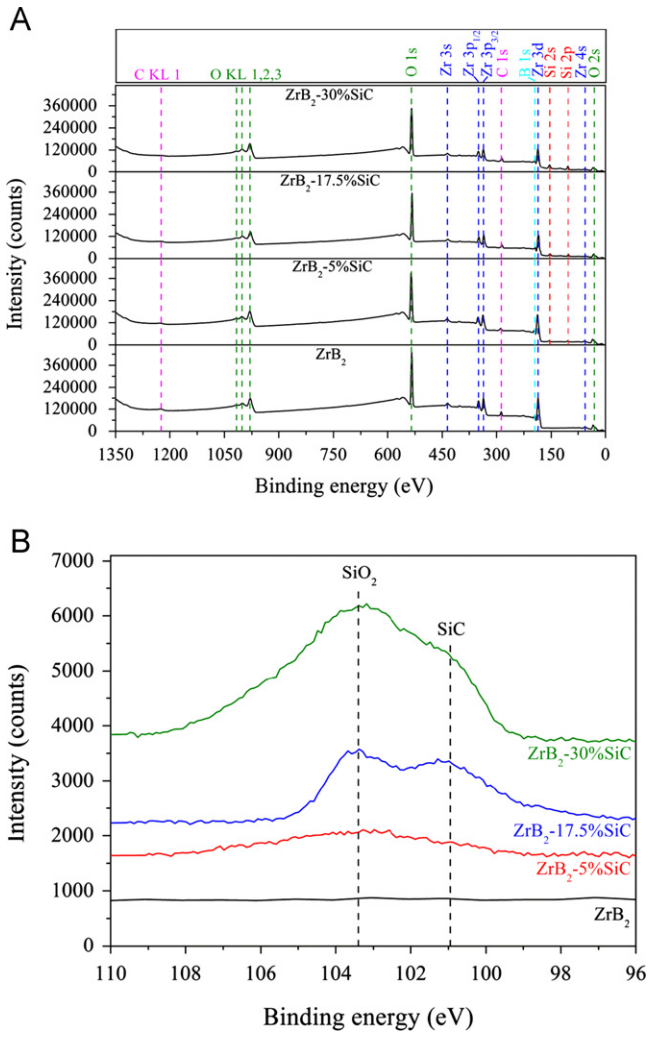

Fig. 11. (A) Survey XPS spectra of the three ZrB_2–SiC powder mixtures (5, 17.5, or 30 vol% SiC) and of the ZrB_2 powder, all subjected to 180 min of high-energy ball-milling. (B) The corresponding high-resolution XPS spectra of the Si 2p (doublet Si $2p_{3/2}$–$2p_{1/2}$) core-level. The peak indexing is included in both figures. No normalization condition was imposed in any of the cases. In (B), the XPS spectra have been shifted along the vertical axis to facilitate their observation. Measurements of signal intensities were made on the original data without shifting.

The proposed mechanism explains well the entire set of experimental observations. Consider first the effect of the SiC content in the ZrB_2–SiC powder mixtures. Clearly, increasing the proportion of SiC particles, the carriers of SiO_2, implies greater formation of borosilicate, and therefore faster SPS kinetics. However, the kinetics enhancement does not scale directly with the SiC content because it is not dictated merely by the pore filling by borosilicate since various diffusion mechanisms are also active. Furthermore, two other reasons are that neither is the pore filling limited by the amount of borosilicate once the pores have collapsed sufficiently, and that the viscosity of borosilicate glasses increases as they become richer in SiO_2 [68]. Consider now the effect of increasing the milling time. Clearly, the greater specific surface area available for passivation resulting from the crystal size refinement entails greater formation of borosilicate, thus inducing, together with the crystal size refinement itself, a faster SPS kinetics. However, the contribution from borosilicate starts to become less relevant with the progressive refinement of the ZrB_2 crystal size to the nanoscale, because in this size regime the sintering kinetics is dominated by the great density of grain boundaries available as fast diffusion paths for the Zr and B species, together with the diminished diffusion lengths. Finally, the faster diffusion induced by the combination of the greater abundance of borosilicate and the smaller crystal sizes also explains the greater coarsening observed with increasing milling time and SiC content, but finer microstructures are obtained since the soaking times required to reach complete densification are shorter.

In closing, it seems worthwhile to discuss potential implications and limitations deriving from the present work. It has been demonstrated recently that the T_{MSC} data provide the referent for the optimization of the SPS isothermal cycles of the ZrB_2 UHTCs. Therefore, thanks to the borosilicate formation, in principle it would be possible to reduce the SPS temperatures of the ZrB_2–SiC powder mixtures to the limits shown in Fig. 3C if the isothermal soaking is appropriate. Such lower-temperature sintering is one of the long sought objectives in the field of UHTCs. However, because the presence of the low melting-point borosilicate segregated at grain boundaries and multi-grain joints will adversely affect the high-temperature mechanical properties [33], the concentration of SiC in the ZrB_2 powder and the milling conditions have to be chosen appropriately for a correct balance between lower-temperature densification and mechanical properties. This warrants further investigation not only on the lower-temperature SPS of these

ZrB_2–SiC powder mixtures, but also on the mechanical properties (and oxidation resistance) of the resulting UHTCs.

5. Conclusions

We have investigated the SPS kinetics of ZrB_2–SiC powder mixtures as a function of the SiC content (5, 17.5, or 30 vol%) and degree of high-energy co-ball-milling. The results allow the following conclusions to be drawn:

1. The SiC addition increasingly enhances the SPS kinetics of ZrB_2 by promoting the formation of amorphous borosilicate that speeds up the interparticle diffusion and is segregated under pressure into the multi-grain joints, thus filling pores. Borosilicate forms due to the reaction during the SPS of the SiO_2 and B_2O_3 existing as passivating layers on the surface of SiC and ZrB_2 particles, respectively.
2. The crystal size refinement induced by the co-milling increasingly enhances the SPS kinetics of the ZrB_2–SiC powder mixtures, which is due to the combination of the reduction of the diffusion distances, the development of a greater density of grain boundaries available as faster diffusion paths, and the greater formation of amorphous borosilicate.
3. The kinetics enhancement promoted by the SiC addition does not scale directly with its content, and becomes less relevant with decreasing ZrB_2 crystal size to the nanoscale. The former finding reflects that the SPS kinetics is not limited by the segregation of borosilicate into the pores (which is also a complex phenomenon not conditioned only by the amount of borosilicate) but involves a combination of various mechanisms, and the latter finding reflects that, at the nanoscale, the SPS kinetics is essentially dictated by the small size of the crystals and its associated effects.
4. The kinetics enhancement promoted by the milling is progressive with the decrease in the crystal size that is achieved, although while it is only moderate with the refinement to the ultra-fine range, it is very abrupt with the refinement to the nanometre range.
5. High-energy ball-milling offers an exciting opportunity to reduce the SPS temperature of ZrB_2–SiC UHTCs. However, because this reduction is derived in part from the presence of amorphous borosilicate segregated at grain boundaries and at multi-grain joints, a judicious selection of the milling conditions and of the SiC content is required to find a proper balance between the lower-temperature densification and the resulting mechanical properties (and oxidation resistance).

Acknowledgements

This work was supported by the Ministerio de Ciencia y Tecnología (Government of Spain) and FEDER funds under Grant no. MAT 2010-16848.

References

[1] W.G. Fahrenholtz, G.E. Hilmas, I.G. Talmy, J.A. Zaykoski, Refractory diborides of zirconium and hafnium, Journal of the American Ceramic Society 90 (5) (2007) 1347–1364.
[2] S.Q. Guo, Densification of ZrB_2-based composites and their mechanical and physical properties: a review, Journal of the European Ceramic Society 29 (6) (2009) 995–1011.
[3] W.C. Tripp, H.H. Davis, H.C. Graham, Effect of an SiC addition on the oxidation of ZrB_2, Journal of the Electrochemical Society 52 (8) (1973) 612–616.
[4] M. Opeka, I.G. Talmy, E.J. Wuchina, J.A. Zaykoski, S.J. Causey, Mechanical, thermal, and oxidation properties of refractory hafnium and zirconium compounds, Journal of the European Ceramic Society 19 (13–14) (1999) 2405–2414.
[5] G.J. Zhang, Z.Y. Deng, N. Kondo, J.F. Yang, T. Ohji, Reactive hot pressing of ZrB_2–SiC composites, Journal of the American Ceramic Society 83 (9) (2000) 2330–2332.
[6] E.J. Opila, M.C. Halbig, Oxidation of ZrB_2–SiC, Ceramic Engineering and Science Proceedings 22 (3) (2001) 221–228.
[7] S.R. Levine, E.J. Opila, M.C. Halbig, J.D. Kiser, M. Singh, J.A. Salem, Evaluation of ultra-high temperature ceramics for aeropropulsion use, Journal of the European Ceramic Society 22 (14–15) (2002) 2757–2767.
[8] F. Monteverde, S. Guicciardi, A. Bellosi, Advances in microstructure and mechanical properties of zirconium diboride based ceramics, Materials Science and Engineering: A 346 (1–2) (2003) 310–319.
[9] A.L. Chamberlain, W.G. Fahrenholtz, G.E. Hilmas, D.T. Ellerby, High-strength zirconium diboride-based ceramics, Journal of the American Ceramic Society 87 (6) (2004) 1170–1172.
[10] F. Monteverde, A. Bellosi, Development and characterization of metaldiboride-based composites toughened with ultra-fine SiC particulates, Solid State Sciences 7 (5) (2005) 622–630.
[11] A.L. Chamberlain, W.G. Fahrenholtz, G.E. Hilmas, Oxidation of ZrB_2–SiC ceramics under atmospheric and reentry conditions, Refractories Applications Transactions 1 (2) (2005) 1–8.
[12] F. Monteverde, Beneficial effects of an ultra-fine α-SiC incorporation on the sinterability and mechanical properties of ZrB_2, Applied Physics A: Materials Science & Processing 82 (2) (2006) 329–337.
[13] A.R. Rezaie, W.G. Fahrenholtz, G.E. Hilmas, Oxidation of zirconium diboride–silicon carbide at 1500 °C a low partial pressure of oxygen, Journal of the American Ceramic Society 89 (10) (2006) 3240–3245.
[14] A. Rezaie, W.G. Fahrenholtz, G.E. Hilmas, Effect of hot pressing time and temperature on the microstructure and mechanical properties of ZrB_2–SiC, Journal of Materials Science 42 (8) (2007) 2735–2744.
[15] A. Rezaie, W.G. Fahrenholtz, G.E. Hilmas, Evolution of structure during the oxidation of zirconium diboride–silicon carbide in air up to 1500 °C, Journal of the European Ceramic Society 27 (6) (2007) 2495–2501.
[16] S.S. Hwang, A.L. Vasiliev, N.P. Padture, Improved processing and oxidation-resistance of ZrB_2 ultra-high temperature ceramics containing SiC nanodispersoids, Materials Science and Engineering: A 464 (1–2) (2007) 216–224.
[17] F. Peng, R.F. Speyer, Oxidation resistance of fully dense ZrB_2 with SiC, $Table_2$, and $TaSi_2$ additives, Journal of the American Ceramic Society 91 (5) (2008) 1489–1494.
[18] G. Inna, J.A. Talmy, M.M. Zaykoski, M. Opeka, High-temperature chemistry and oxidation of ZrB_2 ceramics containing SiC, Si_3N_4, Ta_5Si_3, and $TaSi_2$, Journal of the American Ceramic Society 91 (7) (2008) 2250–2257.
[19] S.C. Zhang, G.E. Hilmas, W.G. Fahrenholtz, Pressureless sintering of ZrB_2–SiC ceramics, Journal of the American Ceramic Society 91 (1) (2008) 26–32.
[20] J.W. Zimmermann, G.E. Hilmas, W.G. Fahrenholtz, Thermal shock resistance of ZrB_2 and ZrB_2–30% SiC, Materials Chemistry and Physics 112 (1) (2008) 140–145.

[21] J. Han, P. Hu, X. Zhang, S. Meng, W. Han, Oxidation-resistant ZrB_2–SiC composites at 2200 °C, Composites Science and Technology 68 (3–4) (2008) 799–806.
[22] J.W. Zimmermann, G.E. Hilmas, W.G. Fahrenholtz, R.B. Dinwiddie, W.D. Porter, H. Wang, Thermophysical properties of ZrB_2 and ZrB_2–SiC ceramics, Journal of the American Ceramic Society 91 (5) (2008) 1405–1411.
[23] S.N. Karlsdottir, J.W. Halloran, Oxidation of ZrB_2–SiC: influence of SiC content on solid and liquid oxide phase formation, Journal of the American Ceramic Society 92 (2) (2009) 481–486.
[24] W.M. Guo, X.J. Zhou, G.J. Zhang, Y.M. Kan, Y.G. Li, P.L. Wang, Effect of Si and Zr additions on oxidation resistance of hot-pressed ZrB_2–SiC composites with polycarbosilane as a precursor at 1500 °C, Journal of Alloys and Compounds 471 (1–2) (2009) 153–156.
[25] W.M. Guo, J. Vleugels, G.J. Zhang, P.L. Wang, O. Van der Biest, Effects of Re_2O_3 (Re = La, Nd, Y and Yb) addition in hot-pressed ZrB_2–SiC ceramics, Journal of the European Ceramic Society 29 (14) (2009) 3063–3068.
[26] P. Hu, W. Guolin, Z. Wang, Oxidation mechanism and resistance of ZrB_2–SiC composites, Corrosion Science 51 (11) (2009) 2724–2732.
[27] J.W. Zimmermann, G.E. Hilmas, W.G. Fahrenholtz, Thermal shock resistance and fracture behavior of ZrB_2-based fibrous monolith ceramics, Journal of the American Ceramic Society 92 (1) (2009) 161–166.
[28] D. Alfano, L. Scatteia, F. Monteverde, E. Bêche, M. Balat-Pichelin, Microstructural characterization of ZrB_2–SiC based UHTC tested in the MESOX plasma facility, Journal of the European Ceramic Society 30 (11) (2010) 2345–2355.
[29] L. Silvestroni, D. Sciti, C. Melandri, S. Guicciardi, Toughened ZrB_2-based ceramics through SiC whisker or SiC chopped fiber additions, Journal of the European Ceramic Society 30 (11) (2010) 2155–2164.
[30] J. Watts, G. Hilmas, W.G. Fahrenholtz, Mechanical characterization of ZrB_2–SiC composites with varying SiC particle sizes, Journal of the American Ceramic Society 94 (12) (2011) 4410–4418.
[31] D. Sciti, S. Guicciardi, L. Silvestroni, SiC chopped fibers reinforced ZrB_2: effect of the sintering aid, Scripta Materialia 64 (8) (2011) 769–772.
[32] D. Sciti, L. Silvestroni, V. Medri, S. Guicciardi, Pressureless sintered in situ toughened ZrB_2–SiC platelets ceramics, Journal of the European Ceramic Society 31 (12) (2011) 2145–2153.
[33] J. Zou, G.J. Zhang, C.F. Hu, T. Nishimura, Y. Sakka, J. Vleugels, O. Van der Biest, Strong ZrB_2–SiC–WC ceramics at 1600 °C, Journal of the American Ceramic Society 95 (3) (2012) 874–878.
[34] D. Sciti, R. Savino, L. Silvestroni, Aerothermal behaviour of a SiC fibre-reinforced ZrB_2 sharp component in supersonic regime, Journal of the European Ceramic Society 32 (8) (2012) 1837–1845.
[35] D. Sciti, L. Silvestroni, Processing, sintering and oxidation behavior of SiC fibers reinforced ZrB_2 composites, Journal of the European Ceramic Society 32 (9) (2012) 1933–1940.
[36] J. Zou, G.J. Zhang, C.F. Hu, T. Nishimura, Y. Sakka, H. Tanaka, J. Vleugels, O. Van der Biest, High-temperature bending strength, internal friction and stiffness of ZrB_2–20 vol% SiC ceramics, Journal of the European Ceramic Society 32 (10) (2012) 2519–2527.
[37] Y. Zhao, L. Wang, G. Zhang, W. Jiang, L. Chen, Preparation and microstructure of a ZrB_2–SiC composite fabricated by the spark plasma sintering–reactive synthesis (SPS–RS) method, Journal of the American Ceramic Society 90 (12) (2007) 4040–4042.
[38] H. Wang, C.A. Wang, X. Yao, D. Fang, Processing and mechanical properties of zirconium diboride-based ceramics prepared by spark plasma sintering, Journal of the American Ceramic Society 90 (7) (2007) 1992–1997.
[39] W.W. Wu, G.J. Zhang, Y.M. Kan, P.L. Wang, K. Vanmeensel, J. Vleugels, O. Van der Biest, Synthesis and microstructural features of ZrB_2–SiC-based composites by reactive spark plasma sintering and reactive hot pressing, Scripta Materialia 57 (4) (2007) 317–320.
[40] X. Zhang, L. Xu, S. Du, C. Liu, J. Han, W. Han, Spark plasma sintering and hot pressing of ZrB_2–SiC_W ultra-high temperature ceramics, Journal of Alloys and Compounds 466 (1–2) (2008) 241–245.
[41] I. Akin, M. Hotta, F.C. Sahin, O. Yucel, G. Goller, T. Goto, Microstructure and densification of ZrB_2–SiC composites prepared by spark plasma sintering, Journal of the European Ceramic Society 29 (11) (2009) 2379–2385.
[42] C.M. Carney, P. Mogilvesky, T.A. Parthasarathy, Oxidation behavior of zirconium diboride silicon carbide produced by the spark plasma sintering method, Journal of the American Ceramic Society 92 (9) (2009) 2046–2052.
[43] W.M. Guo, J. Vleugels, G.J. Zhang, P.L. Wang, O. Van der Biest, Effect of heating rate on densification, microstructure and strength of spark plasma sintered ZrB_2-based ceramics, Scripta Materialia 62 (8) (2010) 802–805.
[44] S. Ran, O. Van der Biest, J. Vleugels, ZrB_2–SiC composites prepared by reactive pulsed electric current sintering, Journal of the European Ceramic Society 30 (12) (2010) 2633–2642.
[45] M. Thompson, W.G. Fahrenholtz, G. Hilmas, Effect of starting particle size and oxygen content on densification of ZrB_2, Journal of the American Ceramic Society 94 (2) (2011) 429–435.
[46] W.M. Guo, Z.G. Yang, J. Vleugels, G.J. Zhang, Effect of pressure loading cycle on spark plasma sintered ZrB_2–SiC–Yb_2O_3 ceramics, Ceramics International 38 (6) (2012) 5293–5297.
[47] L.S. Walker, W.R. Pinc, E.L. Corral, Powder processing effects on the rapid low-temperature densification of ZrB_2, Journal of the American Ceramic Society 95 (1) (2012) 194–203.
[48] S. Zhu, W.G. Fahrenholtz, G.E. Hilmas, S.C. Zhang, Pressureless sintering of carbon-coated zirconium diboride powders, Materials Science and Engineering: A 459 (1–2) (2007) 167–171.
[49] W.G. Fahrenholtz, G.E. Hilmas, S.C. Zhang, S. Zhu, Pressureless sintering of zirconium diboride: particle size and additive effects, Journal of the American Ceramic Society 91 (5) (2008) 1398–1404.
[50] C.A. Galán, A.L. Ortiz, F. Guiberteau, L.L. Shaw, Crystallite size refinement of ZrB_2 by high-energy ball milling, Journal of the American Ceramic Society 92 (12) (2009) 3114–3117.
[51] C.A. Galán, A.L. Ortiz, F. Guiberteau, L.L. Shaw, High-energy ball milling of ZrB_2 in the presence of graphite, Journal of the American Ceramic Society 93 (10) (2010) 3072–3075.
[52] V. Zamora, A.L. Ortiz, F. Guiberteau, L.L. Shaw, M. Nygren, On the crystallite size refinement of ZrB_2 by high-energy ball-milling in the presence of SiC, Journal of the European Ceramic Society 31 (13) (2011) 2407–2414.
[53] P.R. Soni, Mechanical Alloying. Fundamental and Applications, Cambridge International Science Publishing, Cambridge, UK, 2001.
[54] C. Suryanarayana, Mechanical Alloying and Milling, Progress in Materials Science 46 (1–2) (2001) 1–184.
[55] V. Zamora, A.L. Ortiz, F. Guiberteau, M. Nygren, Crystal-size dependence of the spark-plasma-sintering kinetics of ZrB_2 ultra-high-temperature ceramics, Journal of the European Ceramic Society 32 (2) (2012) 271–276.
[56] V. Zamora, A.L. Ortiz, F. Guiberteau, M. Nygren, Spark-plasma sintering of ZrB_2 ultra-high-temperature ceramics at lower temperature via nanoscale crystal refinement, Journal of the European Ceramic Society 32 (10) (2012) 2529–2536.
[57] R.M. German, Sintering Theory and Practice, Wiley, New York, 1996.
[58] R.M. German, Powder Metallurgy Science, Metal Powder Industries Federation, Princeton, New York, 1994.
[59] V. Zamora, A.L. Ortiz, F. Guiberteau, M. Nygren, In-situ formation of ZrB_2–ZrO_2 ultra-high-temperature composites from high-energy ball-milled ZrB_2 powders, Journal of Alloys and Compounds 518 (2012) 38–43.
[60] C. Herring, Effect of change of scale on sintering phenomena, Journal of Applied Physics 21 (4) (1950) 301–303.
[61] A. Lara, A.L. Ortiz, A. Muñoz, A. Domínguez-Rodríguez, Densification of additive-free polycrystalline β-SiC by spark-plasma sintering, Ceramics International 38 (1) (2012) 45–53.
[62] A.L. Ortiz, V. Zamora, F. Rodríguez-Rojas, A study on the oxidation of ZrB_2 powders during high-energy ball-milling in air, Ceramics International 38 (4) (2012) 2857–2863.

[63] A.A. Galuska, J.C. Uht, N. Marquez, Reactive and nonreactive ion mixing of Ti films on carbon substrates, Journal of Vacuum Science & Technology A 6 (1) (1988) 110–122.
[64] L. Huerta, A. Durán, R. Falconi, M. Flores, R. Escamilla, Comparative study of the core level photoemission of the ZrB_2 and ZrB_{12}, Physica C 470 (9–10) (2010) 456–460.
[65] C.D. Wagner, D.E. Passoja, H.F. Hillery, T.G. Kinisky, H.A. Six, W.T. Jansen, J.A. Taylor, Auger and photoelectron line energy relationships in aluminium-oxygen and silicon oxygen compounds, Journal of Vacuum Science & Technology 21 (4) (1982) 933–944.
[66] A.L. Chamberlain, W.G. Fahrenholtz, G.E. Hilmas, Pressureless sintering of zirconium diboride, Journal of the American Ceramic Society 89 (2) (2006) 450–456.
[67] S.C. Zhang, G.E. Hilmas, W.G. Fahrenholtz, Pressureless densification of zirconium diboride with boron carbide additions, Journal of the American Ceramic Society 89 (5) (2006) 1544–1550.
[68] R. Bruckner, J.F. Fernández, Physikalisch-chemische untersuchungen in system B_2O_3-SiO_2, Glastechnische Berichte 39 (1966) 283–293.